tivistic electrons with energy > 20 Mev and > 50 Mev. Channel E3 is the rate from a solid state detector identical to M1 except that a bent aperture in the shield permits direct access of particles that scatter by 45°. Thus E3 is susceptible to the same penetrating electrons that trigger M1 plus nonpenetrating electrons that scatter through the aperture and trigger the 0.4-Mev discriminator. Comparing E3 with C2 and M1 demonstrates the hardening of the electron spectrum toward periapsis, and differencing E3 with M1 demonstrates the loss of the nonpenetrating component below 10 R_J.

Several of the Galilean satellites are immersed in the radiation belts, and there is clear evidence that at least two of them, Io and Europa, influence the trapped particle fluxes. Marks are shown on Fig. 2 where the spacecraft crossed the dipole model magnetic shells containing Io, Europa, and Ganymede. There are prominent dips in the 20-Mev electrons at the Io shell and small fluctuations in the 0.4-Mev electrons. On the other hand, at Europa there are prominent variations in the 0.4-Mev electrons and only small effects in the 20-Mev electrons. An effect at Ganymede is questionable.

Channel M3 is a high energy discriminator on the omnidirectionally shielded solid state detector. Set high enough to have low ($< 2 \times 10^{-3}$) efficiency for electrons, this discriminator is efficient for protons between 70 and 150 Mev. The M3 response seen in Fig. 2 is caused partly by single electrons at low efficiency, partly by double coincidence of electrons, and partly by protons. When the appropriate linear and quadratic terms in M1 that represent electron background are subtracted from M3, one is left with two proton peaks, one at 0100, one at 0300, with a relative minimum between them. The second peak is clearly visible in the figure. These peaks are at the inbound and outbound crossings of the $L = 3.6$ shell, and the maximum proton intensity is $J_0 = 2.5 \times 10^4$ cm^{-2} sec^{-1}. These peaks represent the only proton fluxes visible to our counters during the flyby.

Particle identification features in the instrument design were successful in separating electrons from protons, and we name the particle species with confidence. Specifically, one of our detectors was a Cerenkov counter sensitive only to particles with velocity greater than $0.75c$ (for example, C2 in Fig. 2). There is evidence against significant proton fluxes above this energy (450 Mev) and so the counts are known to be electrons. Comparisons between the Cerenkov counter and channel M1 are in agreement, and because M3 found so few protons, M1 counted essentially all electrons.

Flux values and energy ranges are preliminary as we have not yet made proper integrations of the particle spectra over the detector responses. Therefore these numbers should be given an uncertainty of about 50 percent.

More serious data misinterpretation could arise from spacecraft charging. The expected average photoelectron flux is similar to the measured fluxes of energetic electrons inside 10 R_J. This means that, unless there is an unmeasured cold plasma component, the spacecraft may need to assume a large negative potential in order to maintain zero net current (*3*). Until it can be shown that Pioneer 10 was not driven to megavolt potentials, the present measurements cannot be safely assumed to correspond to the ambient Jovian particle fluxes. The relative absence of 0.1- to 2-Mev electrons is not firm evidence for spacecraft charging, as this would be expected for a relativistic Maxwellian distribution with a temperature over 5 Mev.

In conclusion, we note that the presence of very energetic electrons in the magnetodisk cannot be easily explained in terms of solar wind injection and convective acceleration. As an alternative, we would like to point out that interactions with the nonrotating solar wind may cause a differential rotation between the planet and the outer magnetodisk which in turn can lead to large electric fields parallel to the magnetic field lines. The expected sign and magnitude of these electric fields is such that photoelectrons in the Jovian atmosphere could be accelerated outward to very high energies. Presumably the angular distributions measured by the various detectors on Pioneer 10 will provide clues to the true nature of the injection and acceleration processes.

R. WALKER FILLIUS
CARL E. MCILWAIN
University of California, San Diego, La Jolla 92037

References and Notes

1. J. H. Wolfe, H. R. Collard, J. D. Mihalov, D. S. Intriligator, *Science* **183**, 303 (1974).
2. E. J. Smith, L. Davis, Jr., D. E. Jones, D. S. Colburn, P. J. Coleman, P. Dyal, C. P. Sonett, *ibid.*, p. 305.
3. S. E. DeForest, *J. Geophys. Res.* **77**, 651 (1972).
4. We thank G. E. Peters, E. W. Strein, and G. W. Schmidt of the University of California, San Diego, for their help in developing the instrumentation and the data reduction programs, and we thank C. F. Hall and D. Porter of the NASA/Ames Research Center for their support. This work was supported by NASA contracts NAS 2-5602 and NAS 2-6552, and by NASA grant NGL 05-005-007.

21 December 1973

Pioneer 10 Infrared Radiometer Experiment: Preliminary Results

Abstract. *Thermal maps of Jupiter at 20 and 40 micrometers show structure closely related to the visual appearance of the planet. Peak brightness temperatures of 126° and 145°K have been measured on the South Equatorial Belt, for the 20- and 40-micrometer channels, respectively. Corresponding values for the South Tropical Zone are 120° and 138°K. No asymmetries between the illuminated sunlit and nonilluminated parts of the disk were found. A preliminary discussion of the data, in terms of simple radiative equilibrium models, is presented. The net thermal energy of the planet as a whole is twice the solar energy input.*

The Jupiter Pioneer 10 infrared radiometer experiment was designed to map the planet in two wavelength ranges. On the basis of the knowledge that the thermal opacity of the Jovian atmosphere is provided mostly by the pressure-induced dipole absorption of H_2, the range from 14 to 25 μm (20-μm channel) was selected to isolate the rotational component of the H_2 spectrum. The range from 30 to 55 μm (40-μm channel) was also chosen because it contains the translational component of the H_2 spectrum, which depends on the partial pressure of He (*1*). With the channels chosen in this fashion, the sum of the powers measured in the two channels provides a measure of the net energy output, and their ratio provides a measure of a, the abundance ratio of He to H_2 by number (*2*). From only two radiance

Table 1. Measured and predicted thermal parameters of the Jovian atmosphere.

Region	Measured						Predicted	
	T (20 μm) (°K)	T (40 μm) (°K)	T_e (°K)	a	d (20 μm)	d (40 μm)	d (20 μm)	d (40 μm)
SEB	126	145	133	0.6	0.40	0.34	0.65	0.36
STZ	120	138	126	0.8	0.62	0.33	0.68	0.37

measurements a value of a can be inferred on the basis of a model for the temperature-pressure profile of the atmosphere. The only observable available to constrain the adopted model atmosphere is the darkening, measured at both wavelengths, toward the limb; the atmosphere must be considered approximately homogeneous in longitude. In this report we present the preliminary results obtained during the Pioneer 10 encounter and compare them with predictions of simple models calculated a priori.

The radiometer consists, briefly, of a reflecting telescope with a 3-inch (7.6-cm) aperture mounted rigidly on the spacecraft. Planet coverage is obtained by the spin and orbital motion of the spacecraft. The field stops for both channels are rectangular, with dimensions 17 by 6 mrad, elongated in the direction of roll motion. The spectral filtering has been effected by reflections from reststrahlen filters and transmission through $f/1$ field lenses of Irtran-6 and Si. The detectors are 88-junction circular arrays of thermopiles. The radiometric scale is set by a zero established when viewing space and by the response to a calibrator plate at known temperature, interposed once in each roll cycle. The dwell time of each measurement was fixed at 38 msec, based on consideration of the detector time constant, the smear produced by spin, and the aperture dimensions. The radiometer behavior during the cruise phase was monitored periodically, and its noise and scale remained sensibly unchanged during encounter. The telemetered data, digitized to 8 bits, have been converted into irradiances on the basis of prelaunch laboratory calibrations of instrumental response to blackbodies at known and controllable temperatures.

The planet viewing period was fixed by orbit geometry between $2^h\ 11^m$ and $0^h\ 49^m$ before periapsis. In each of the roll cycles covering the planetary disk, a maximum of 33 planet irradiances were obtained in one channel. These measurements just sufficed to provide coverage of the Jovicentric longitude (system II) range 250° to 360°. In Figs. 1 and 2 we give the contours of equal brightness temperatures as they would have appeared from a point midway through the observation period. The data points obtained actually show a wealth of small structure detail which has been smoothed out by the interpolation procedure employed in constructing the isotherms. A brightness temperature profile through the subspacecraft point at the midpoint is also shown. Some features shown by the isotherms, elongated in the roll direction, are artifacts introduced by the use of preliminary trajectory and roll timing parameters. These geometrical factors, together with the nonsynchronicity of the spacecraft spin period with the timing of the planet data-taking cycle, are critical near the limb of the planet. Nevertheless, the contours are explicit and realistic enough to show the large-scale thermal structure of the atmosphere and the relation it has to its visible appearance. In particular,

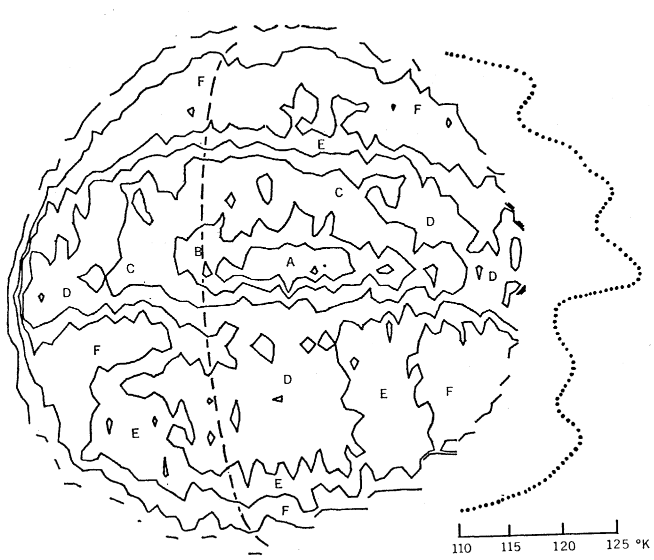

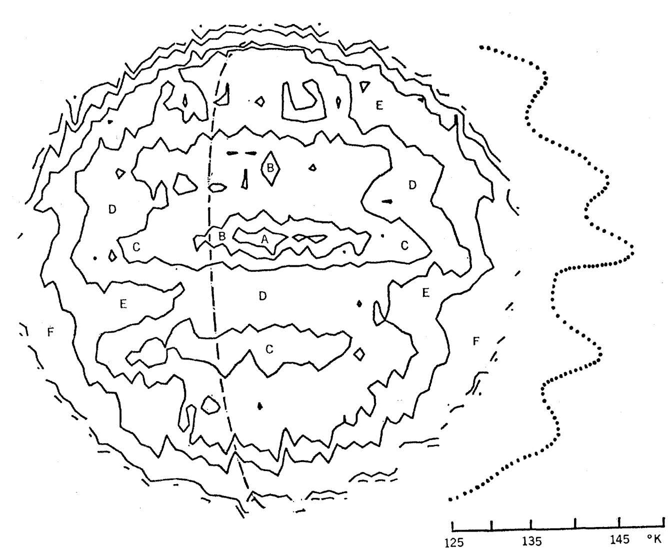

Fig. 1 (left). Contours of equal brightness temperature for the 20-μm channel, drawn on a conical projection of the planet as seen from a point on the trajectory with subspacecraft planetocentric coordinates (system II) 303° longitude and −11° latitude. The dashed line represents the terminator. Contours labeled A, B, C, D, E, and F enclose regions with brightness temperatures higher than or equal to 125°, 124°, 123°, 121°, 119°, and 115°K, respectively. North is at the top. Fig. 2 (right). Same as Fig. 1, but for the 40-μm channel. Contours A, B, C, D, E, and F enclose regions with brightness temperatures higher than or equal to 144°, 141°, 138°, 134°, 130°, and 115°K, respectively.

the data show that, as expected, the illuminated and nonilluminated sides have the same brightness temperatures. The South Equatorial Belt (SEB) shows the highest brightness temperatures and appears separated from the North Equatorial Belt by the incipiently resolved equatorial zone. The South Tropical Zone (STZ) is clearly noticeable because of its low brightness temperature and large degree of limb darkening. Further south, the increase of temperature associated with the South Temperate Belt is also shown. A more detailed comparison with the visual images will be carried out when definitive geometry has been established.

In this preliminary discussion we shall characterize the thermal emission of the two most prominent features, the SEB and STZ, by a mean intensity at normal emergency b_1 and a coefficient of linear limb darkening d. The surface brightness at an emission angle e is then related to these two parameters by

$$b(e) = b_1 (1 - d + d \cos e)$$

The values of the mean peak brightness temperatures, corresponding to b_1, and the best-fit darkening coefficients for each region and each channel are given in Table 1. In order to compare these parameters with predicted values, we have calculated values of b_1 and d for a family of model atmospheres as calculated by Trafton (*3*), characterized by an effective temperature T_e and an abundance ratio a, which essentially determines the opacity. A NH_3 equilibrium concentration has been included to evaluate its contribution to the opacity, although it is of secondary importance. On the basis of these models, we infer the effective temperatures and nominal He abundances given in Table 1. The comparison of the calculated darkening coefficients, fixed by the model, with the measured ones, however, shows a conspicuous disagreement in the 20-μm channel, especially for the SEB. This implies that the calculated temperature gradient, with respect to optical depth in the 20-μm channel, is too high. Since darkening in the 40-μm channel is approximately as predicted, the lapse rate calculated on the assumption of radiative-convective equilibrium should be approximately correct, and the disagreement found implies that the opacity in the 20-μm channel has been underestimated.

The values of the effective temperatures derived for the SEB and the STZ will not be affected significantly by a more realistic evaluation of the opacity in the 20-μm channel. If we take into consideration the fact that the fraction of the planet covered by zones and polar regions is larger than that covered by the SEB and other belts, generally of lower net thermal flux than the SEB, it is estimated that the whole planet has an effective temperature close to $T_e = 128°K$. If we adopt a Bond albedo of 0.42, the effective temperature Jupiter would attain if heated only by insolation is $T_e = 107° \pm 3°K$. We thus derive a net energy output between 2.0 and 2.5 times larger than the solar energy input. This value is somewhat smaller than that inferred from aircraft-based measurements of the planet as a whole (*4*). The main uncertainty remaining in this important characteristic of the Jupiter interior arises from the estimates of the planetary Bond albedo.

S. C. CHASE, R. D. RUIZ
Santa Barbara Research Center, Santa Barbara, California
G. MÜNCH, G. NEUGEBAUER
M. SCHROEDER
California Institute of Technology, Pasadena 91103
L. M. TRAFTON
University of Texas, Austin 78712

References and Notes

1. L. M. Trafton and G. Münch, *J. Atmos. Sci.* **26**, 813 (1969).
2. D. M. Hunten and G. Münch, *Space Sci. Rev.* **14**, 433 (1973).
3. L. M. Trafton, *Astrophys. J.* **147**, 765 (1967).
4. H. H. Aumann, C. M. Gillespie, F. J. Low, *Astrophys. J. Lett.* **157**, 69 (1969).
5. We thank J. Bennett for her efforts in the programming and data reduction. The cooperation of all the personnel of the Pioneer Project is also gratefully acknowledged.

21 December 1973

Pioneer 10 Observations of the Ultraviolet Glow in the Vicinity of Jupiter

Abstract. *A two-channel ultraviolet photometer aboard Pioneer 10 has made several observations of the ultraviolet glow in the wavelength range from 170 to 1400 angstroms in the vicinity of Jupiter. Preliminary results indicate a Jovian hydrogen (1216 angstrom) glow with a brightness of about 1000 rayleighs and a helium (584 angstrom) glow with a brightness of about 10 to 20 rayleighs. In addition, Jupiter appears to have an extensive hydrogen torus surrounding it in the orbital plane of Io. The mean diameter of the torus is about equal to the diameter of the orbit of Io. Several observations of the Galilean satellites have also occurred but only a rather striking Io observation has been analyzed to date. If the observed Io glow is predominantly that of Lyman-α, the surface brightness is about 10,000 rayleighs.*

The ultraviolet instrument (*1*) on Pioneer 10 is a two-channel photometer designed to observe the resonance emissions from atomic hydrogen and helium at 1216 Å (the H Lyman-α line) and 584 Å, respectively. The instrument uses a filter and photocathodes to isolate these two emission features.

Detailed calculations (*2*) show that the hydrogen and helium resonance lines are the strongest features to be expected from the outer atmosphere of Jupiter, and arise from resonance scattering of the incident solar hydrogen and helium lines; thus, only broadband isolation of these lines is required. The He channel uses a thin aluminum film as a filter and LiF as a photocathode, resulting in a spectral band pass of approximately 200 to 800 Å. The hydrogen channel uses the front surface of the Al film as a photocathode for which the photoelectric response extends up to about 1400 Å. This channel is sensitive to both hydrogen and helium emissions, but the former is more intense by more than an order of magnitude, so the recorded signals accurately represent the Lyman-α intensity.

The optical axis of the photometer is oriented at 20° to the spacecraft spin axis while the instantaneous field of view is approximately 1° by 20° with the longer dimension tangential to the 20° arc swept out by the spacecraft rotation.

This orientation was chosen to give two views of Jupiter, the first occurring at approximately 50 Jovian radii (R_J), and outside the predicted radiation belts, while the second observation period occurred at about 10 R_J. In addition, several observations of the Galilean satellites were possible during the 5 days before closest approach.